Vortex Formation in Ellipsoidal Thermal Bubbles

ALAN SHAPIRO AND KATHARINE M. KANAK*

School of Meteorology, University of Oklahoma, Norman, Oklahoma

(Manuscript received 6 June 2001, in final form 30 January 2002)

ABSTRACT

The rise of an isolated dry thermal bubble in a quiescent unstratified environment is a prototypical natural convective flow. This study considers the rise of an isolated dry thermal bubble of ellipsoidal shape (elliptical in both horizontal and vertical cross sections). The azimuthal asymmetry of the bubble allows the vorticity tilting mechanism to operate without an environmental wind. The dry Boussinesq equations of motion are solved analytically as a Taylor series in time for the early time behavior of the bubble (involving derivatives of up to the third order in time). The analytic results are supplemented with numerical simulations to examine the longer-time behavior. The first nonzero term in the Taylor expansion for the vertical vorticity is a third-order term, and appears as a four-leaf clover pattern with lobes of alternating sign. The horizontal flow associated with this vorticity pattern first appears as a sheared stagnation point-type flow, but eventually organizes into vertical vortices that fill the bubble. The vortices induce large structural changes to the bubble and eventually reverse the sense of the azimuthal asymmetry.

1. Introduction and background

Natural (free) convective flows abound in nature and technology. Examples include flows induced by lit cigarettes, computer CPUs, electronic circuitry, radiator fins, charcoal grills, and the heated ground. The structure of the convective atmospheric boundary layer is dependent, in part, on the statistical structure of individual and mutually interacting convective elements, and on the interactions between convective elements and the environmental wind. Many of these and other natural convective flows are azimuthally asymmetric. However, because even the most idealized natural convective entities are intrinsically nonlinear (fluid inertia and the coupling between dynamical and thermodynamical variables are essential aspects of the problem), they have been difficult to analyze theoretically without considering their ensemble characteristics to be axisymmetric or slab-symmetric. The present study is one of the first to focus on the impact of asymmetrical geometry (ellipticity in both horizontal and vertical cross sections) on the behavior of an isolated thermal bubble. The azimuthal ellipticity allows the vorticity tilting mechanism to operate even in the absence of wind shear. The subsequent development of vertical vortices and associated structural changes to the bubble are the main features of interest in this investigation. It should be kept in mind that much of the current impetus for thermal convection research is the need for quantitative measures of entrainment in thermals and convective clouds, processes in which vorticity and vortices play a primary role (Turner 1986; Morton 1997a). Although our study does not focus on entrainment per se, the ideas presented herein may prove useful in improving theories of entrainment.

Early conceptual models of natural atmospheric convection focussed on plumes, which are spatially continuous buoyant regions arising from a maintained point or line source of buoyancy, and on thermals, which are discrete buoyant elements confined to a finite volume that arise from an impulsive source of buoyancy (Emanuel 1994). The notion that these simple convective elements arose from point or line singularities (or from virtual singularities) simplified laboratory analyses and led to the early development of simple but extremely powerful similarity theories.

The classical conceptual model for the plume describes a steady state flow that laterally entrains ambient fluid as it ascends. Entrainment has been an important part of most theories of atmospheric convection since Stommel (1947) observed that Caribbean cloud temperatures were very close to environmental temperatures and concluded that the isolated parcel theory of convection was not entirely correct. Stommel postulated the idea of continuous lateral entrainment to explain these observations (Stommel 1947, 1951; Houze 1993). En-

* Current affiliation: Cooperative Institute for Mesoscale Meteorological Studies, University of Oklahoma, Norman, Oklahoma.

Corresponding author address: Dr. Alan Shapiro, University of Oklahoma, 100 E. Boyd, Room 1310, Norman, OK 73019.
E-mail: ashapiro@ou.edu

trainment in clouds other than trade cumuli was first documented by Byers and Braham (1949).

The advancing plume is typically considered to be conical in shape and can be laminar or turbulent. For example, rising smoke from a cigarette is often laminar up to a threshold height at which the Reynolds number becomes large enough that the plume becomes turbulent (Scorer and Ludlum 1953). Beginning in the 1950s, theoretical studies of natural convection used similarity models (justified by dimensional analysis) to describe the dynamical structure of laminar and turbulent plumes (Yih 1951, 1977; Rouse et al. 1952; Batchelor 1954; Morton et al. 1956; Turner 1962, 1963a,b, 1969; Yih and Wu 1981). Laboratory experiments were undertaken to confirm these analyses and to obtain numerical values of coefficients that could not be estimated from the theories (e.g., Yih 1951; Rouse et al. 1952; Morton et al. 1956; Turner 1986). However, a wide range of these values has been measured, and universal constants are still lacking (Morton 1997a). Numerical simulations of maintained sources of buoyancy were performed by Lilly (1962, 1964) for a line source, and by Ogura (1962) for an axisymmetric source.

The phenomenon of plume merger from multiple buoyancy sources was illustrated by Rouse et al. (1953), Briggs (1975), and others. Plumes in close proximity to one another will entrain each other and, at some height above the source, behave as a single plume located midway between the sources. This was also found to be the case for numerically simulated thermals (Wilkens et al. 1976). Morton (1997b) describes a laboratory experiment in which a two-dimensional linelike thermal breaks down into a line of pointlike thermals that merge together as they move vertically through the tank. Convective cloud mergers have been investigated numerically by Tao and Simpson (1989), Shapiro and Kogan (1994), and Kogan and Shapiro (1996). These studies suggest that the dynamics of convective cloud mergers may be more complex than that of dry convective mergers. The Shapiro and Kogan (1994) study was noteworthy in that it showed the production of vertical vortices on the periphery of three merging axisymmetric convective clouds in a shear-free environment. The viewpoint that those multiple individually axisymmetric elements can be conceptualized as a single asymmetric element partially motivated the present work, although the dry single-bubble framework of the present study is simpler and permits a more rigorous analysis than was possible in the three-cloud scenario.

Scorer and Ludlum (1953) proposed a bubble theory of cumulus development in which convection was considered as a series of successive bubbles. As the first bubble rises, it mixes with the environmental air and leaves behind a wake composed of both bubble and environmental air. This wake constitutes a preferred region for the ascent of succeeding bubbles because the bubble–environmental air mix is less effective in diluting new bubbles than pure environmental air. Central to this theory is the notion that bubbles are eroded by the environment (entrainment). Ludlam (1958) also suggested that an individual thermal could grow continuously in size by entrainment. The bubble theory of convection may be considered an extension of the classical parcel theory to include the interaction of the bubble with its environment (Levine 1959; Ogura 1963).

Further development of the bubble theory of convection was presented by Levine (1959) and Turner (1963b), who suggested that the rising thermal is characterized by a spheroidal vortex or azimuthal vortex ring, and applied Hill's spherical vortex solution (Lamb 1945). Laboratory experiments by Scorer (1957), Turner (1957), and Woodward (1959) also exhibited this azimuthal vortical structure. Morton (1997a) states that vorticity plays a crucial role in entrainment, and that thermals and spheroidal vortices differ not in the existence of mean azimuthal vorticity but in its distribution.

The structure of thermals and plumes in a stably stratified environment have been considered by Morton et al. (1956), Richards (1961), Turner (1963b), and others. Successive thermals rising through nonrotating (Wilkens et al. 1972) and rotating environments were studied experimentally (Wilkens et al. 1971a) and numerically (Wilkens et al. 1971b).

More recently, the evolution of thermals started from rest were studied experimentally and numerically by Sánchez et al. (1989) in stratified and nonstratified environments. That study focussed on the early transient (laminar) stage of the flow, prior to the development of turbulence and self-similarity. The pre-self-similar thermal had a lower entrainment rate than that of a self-similar thermal. Interfacial instabilities on moist thermals started from rest were investigated numerically by Grabowski and Clark (1991, 1993a,b). Their analyses suggested that turbulent entrainment in cumulus clouds was largely due to shear-induced instabilities at the cloud–environment interface, with the shear arising from an inviscid baroclinic process. Experiments with moist thermals rising in sheared and unsheared environments suggested that the dynamics of the interface was only slightly affected by environmental shear for typical atmospheric values of the shear rate. The interface instability process was affected mostly by the buoyancy and velocity fields in the immediate vicinity of the interface, not by the larger-scale (environmental) variations in the flow. However, gross features of the thermal such as the orientation of the mushroom-shaped ''cap'' were affected by the shear.

This study is concerned with the early transient (laminar) behavior of ellipsoidal thermal bubbles in an unstratified quiescent environment. We assume the spatial scales of the flow are small enough that the Coriolis force can safely be neglected, and that density variations are small enough that the Boussinesq approximation is valid. For simplicity we also neglect diffusion. Although our results will show that inviscid dynamics are sufficient to produce vertical vorticity (and vortices) in the

bubble, we should bear in mind that diffusion would likely become important as the temperature and velocity gradients near the leading edge of the rising bubble (and on the sides of the bubble as the vortices develop) increase in magnitude. We speculate that the process of vortex generation described herein would still occur in a viscous fluid but that the details of the flow (e.g., intensity and scale of the vortices) would likely be modified.

In the next section we introduce the governing equations for dry Boussinesq inviscid convective flow, and consider a perturbation analysis (Taylor series expansion in time) for the evolution of dry convective elements at early times. In section 3, the perturbation analysis is applied to a grid of thermal bubbles and to an isolated thermal bubble. A key result for the isolated bubble is the prediction for nonzero vertical vorticity to appear as a third-order effect with a clover-leaf pattern in the horizontal. The analytic results are complemented with numerical simulation results in section 4. The numerical results confirm the early time analytic results and show that the vertical vorticity is eventually organized into well defined vortices (and later, subvortices) that evolve with the growing thermal bubble. A brief summary and a discussion of future work follow in section 5.

2. Governing equations

a. Equations for dry Boussinesq thermal convection

The rise of ellipsoidal thermal bubbles in an unstratified atmosphere otherwise at rest is investigated. With diffusion and the Coriolis force neglected, the dry Boussinesq equations of motion, mass conservation (incompressibility condition), and thermodynamic energy reduce to

$$\frac{\partial u}{\partial t} + (\mathbf{v}\cdot\boldsymbol{\nabla})u = -\frac{\partial \Pi}{\partial x}, \tag{2.1}$$

$$\frac{\partial v}{\partial t} + (\mathbf{v}\cdot\boldsymbol{\nabla})v = -\frac{\partial \Pi}{\partial y}, \tag{2.2}$$

$$\frac{\partial w}{\partial t} + (\mathbf{v}\cdot\boldsymbol{\nabla})w = g\alpha T - \frac{\partial \Pi}{\partial z}, \tag{2.3}$$

$$\frac{\partial u}{\partial x} + \frac{\partial v}{\partial y} + \frac{\partial w}{\partial z} = 0, \tag{2.4}$$

$$\frac{\partial T}{\partial t} + (\mathbf{v}\cdot\boldsymbol{\nabla})T = 0. \tag{2.5}$$

Here, x, y, and z are Cartesian coordinates, u, v, and w are the corresponding velocity components; and $\mathbf{v} \equiv u\mathbf{i} + v\mathbf{j} + w\mathbf{k}$ is the velocity vector. The perturbation temperature T is the departure of temperature from a constant reference value. The perturbation pressure (departure of pressure from a hydrostatic reference state) divided by a constant reference density is denoted by Π and will be referred to hereafter simply as the perturbation pressure. For a perfect gas, the coefficient of thermal expansion α is the reciprocal of the absolute temperature. Under the Boussinesq approximation we treat α as constant.

A diagnostic equation for the pressure is obtained by taking the divergence of the vector form of the equations of motion (2.1)–(2.3) and applying the incompressibility condition (2.4):

$$\nabla^2\Pi = g\alpha\frac{\partial T}{\partial z} - \boldsymbol{\nabla}\cdot[(\mathbf{v}\cdot\boldsymbol{\nabla})\mathbf{v}]. \tag{2.6}$$

Cross differentiating the component equations of motion (2.1)–(2.3) results in the x, y, and z component vorticity equations:

$$\frac{\partial \xi}{\partial t} + (\mathbf{v}\cdot\boldsymbol{\nabla})\xi - (\boldsymbol{\omega}\cdot\boldsymbol{\nabla})u = g\alpha\frac{\partial T}{\partial y}, \tag{2.7a}$$

$$\frac{\partial \eta}{\partial t} + (\mathbf{v}\cdot\boldsymbol{\nabla})\eta - (\boldsymbol{\omega}\cdot\boldsymbol{\nabla})v = -g\alpha\frac{\partial T}{\partial x}, \tag{2.7b}$$

$$\frac{\partial \zeta}{\partial t} + (\mathbf{v}\cdot\boldsymbol{\nabla})\zeta - (\boldsymbol{\omega}\cdot\boldsymbol{\nabla})w = 0. \tag{2.8}$$

Here $\xi \equiv \partial w/\partial y - \partial v/\partial z$, $\eta \equiv \partial u/\partial z - \partial w/\partial x$, and $\zeta \equiv \partial v/\partial x - \partial u/\partial y$, are the x, y, and z components of vorticity, respectively, and $\boldsymbol{\omega} \equiv \xi\mathbf{i} + \eta\mathbf{j} + \zeta\mathbf{k}$ is the vorticity vector. Equations (2.7a) and (2.7b) can be combined as

$$\frac{\partial \boldsymbol{\omega}_H}{\partial t} + (\mathbf{v}\cdot\boldsymbol{\nabla})\boldsymbol{\omega}_H - (\boldsymbol{\omega}\cdot\boldsymbol{\nabla})\mathbf{v}_H = -g\alpha\mathbf{k}\times\boldsymbol{\nabla}_H T. \tag{2.9}$$

Here, $\boldsymbol{\omega}_H \equiv \xi\mathbf{i} + \eta\mathbf{j}$ is the horizontal vorticity vector, $\mathbf{v}_H \equiv u\mathbf{i} + v\mathbf{j}$ is the horizontal velocity vector, and $\boldsymbol{\nabla}_H \equiv \mathbf{i}\partial/\partial x + \mathbf{j}\partial/\partial y$ is the horizontal gradient operator.

b. Taylor series expansion

A useful device for describing the early time behavior of flows originating from idealized initial conditions is to decompose the flow variables into a Taylor series in time. If the initial conditions are simple enough, it may be possible to obtain the spatially varying expansion coefficients analytically, at least for low orders of time. Such a procedure has been used, for example, in Taylor and Green's (1937) analysis of the turbulent breakdown of large eddies, and in Adem's (1956) study of vortex motion on a beta plane.

We begin by expanding each dependent variable into a Taylor series of the form

$$\begin{aligned}\phi(x, y, z, t) &= \tilde{\phi}^0(x, y, z) + t\tilde{\phi}^1(x, y, z) + t^2\tilde{\phi}^2(x, y, z) \\ &\quad + t^3\tilde{\phi}^3(x, y, z) + \cdots,\end{aligned} \tag{2.10}$$

where

$$\tilde{\phi}^m(x, y, z) \equiv \frac{1}{m!}\frac{\partial^m \phi}{\partial t^m}(x, y, z, 0). \tag{2.11}$$

In this approach the zeroth-order variables are the initial conditions; the first-order variables are the initial rates of change (initial tendencies); the second-order variables are, apart from a factor of one-half, the initial rates of change of the tendencies; and so forth.

Substituting (2.10) into (2.1)–(2.3), (2.5), (2.6), (2.8), and (2.9), and collecting terms in like-order of time, we obtain a hierarchy of governing equations. Assuming the atmosphere is initially at rest, the equations for the lowest-order variables are as follows.

Equations for zeroth-order variables are

$$\tilde{T}^0 = T(x, y, z, 0), \tag{2.12a}$$

$$\nabla^2\tilde{\Pi}^0 = g\alpha\frac{\partial\tilde{T}^0}{\partial z}, \tag{2.12b}$$

$$\tilde{\mathbf{v}}_H^0 = \tilde{\boldsymbol{\omega}}_H^0 = \tilde{w}^0 = \tilde{\zeta}^0 = 0. \tag{2.12c}$$

Equations for first-order variables are

$$\tilde{\mathbf{v}}_H^1 = -\boldsymbol{\nabla}_H\tilde{\Pi}^0, \tag{2.13a}$$

$$\tilde{w}^1 = -\frac{\partial\tilde{\Pi}^0}{\partial z} + g\alpha\tilde{T}^0, \tag{2.13b}$$

$$\tilde{\boldsymbol{\omega}}_H^1 = -g\alpha\mathbf{k}\times\boldsymbol{\nabla}_H\tilde{T}^0, \tag{2.13c}$$

$$\tilde{T}^1 = \tilde{\Pi}^1 = \tilde{\zeta}^1 = 0. \tag{2.13d}$$

Equations for second-order variables are

$$2T^2 = -\tilde{\mathbf{v}}^1\cdot\boldsymbol{\nabla}\tilde{T}^0, \tag{2.14a}$$

$$\nabla^2\tilde{\Pi}^2 = g\alpha\frac{\partial\tilde{T}^2}{\partial z} - \boldsymbol{\nabla}\cdot[(\tilde{\mathbf{v}}^1\cdot\boldsymbol{\nabla})\tilde{\mathbf{v}}^1], \tag{2.14b}$$

$$\tilde{\mathbf{v}}_H^2 = \tilde{\boldsymbol{\omega}}_H^2 = \tilde{w}^2 = \tilde{\zeta}^2 = 0. \tag{2.14c}$$

Equations for third-order variables are

$$3\tilde{\mathbf{v}}_H^3 = -(\tilde{\mathbf{v}}^1\cdot\boldsymbol{\nabla})\tilde{\mathbf{v}}_H^1 - \boldsymbol{\nabla}_H\tilde{\Pi}^2, \tag{2.15a}$$

$$3\tilde{w}^3 = -(\tilde{\mathbf{v}}^1\cdot\boldsymbol{\nabla})\tilde{w}^1 - \frac{\partial\tilde{\Pi}^2}{\partial z} + g\alpha\tilde{T}^2, \tag{2.15b}$$

$$3\tilde{\boldsymbol{\omega}}_H^3 = -(\tilde{\mathbf{v}}^1\cdot\boldsymbol{\nabla})\tilde{\boldsymbol{\omega}}_H^1 + (\tilde{\boldsymbol{\omega}}^1\cdot\boldsymbol{\nabla})\tilde{\mathbf{v}}_H^1 - g\alpha\mathbf{k}\times\boldsymbol{\nabla}_H\tilde{T}^2, \tag{2.15c}$$

$$3\tilde{\zeta}^3 = (\tilde{\boldsymbol{\omega}}_H^1\cdot\boldsymbol{\nabla})\tilde{w}^1 = g\alpha(\mathbf{k}\times\boldsymbol{\nabla}_H\tilde{T}^0)\cdot\boldsymbol{\nabla}_H\frac{\partial\tilde{\Pi}^0}{\partial z}$$

$$= g\alpha\mathbf{k}\cdot\left(\boldsymbol{\nabla}_H\tilde{T}^0\times\boldsymbol{\nabla}_H\frac{\partial\tilde{\Pi}^0}{\partial z}\right), \tag{2.15d}$$

$$\tilde{T}^3 = \tilde{\Pi}^3 = 0. \tag{2.15e}$$

c. Discussion

The equations for zeroth-order variables consist of a specified initial thermal field (2.12a) and an elliptic equation for the pressure (2.12b). This pressure field is induced by the buoyancy force and supports the accelerations necessitated by mass conservation.

The first-order vertical velocity is forced by the zeroth-order buoyancy and the zeroth-order vertical pressure gradient force (2.13b). Since the first-order horizontal flow (2.13a) is equal to the gradient of (minus) zeroth-order pressure, it is irrotational and thus there is no first-order vertical vorticity. However, there is first-order baroclinically generated horizontal vorticity (2.13c); the horizontal vorticity vectors are tangent to the isotherms. When the initial thermal field is prescribed as an isolated thermal bubble, these first-order variables describe the tendency to produce an ''in–up–out'' flow we will refer to as the basic meridional circulation.

The equations for second-order variables describe the thermodynamic response to the first-order basic meridional circulation. The second-order temperature is forced by the advection of the zeroth-order temperature by the basic meridional circulation (2.14a). The second-order pressure field responds to this second-order buoyancy forcing and to the divergence of first-order acceleration terms associated with the basic meridional circulation (2.14b).

The third-order horizontal flow responds to the second-order pressure gradient force and to the self-advection of the horizontal component of the basic meridional circulation by the basic meridional circulation (2.15a). The third-order vertical velocity is forced by an imbalance between the second-order pressure gradient force, second-order buoyancy, and self-advection of the first-order vertical velocity (2.15b). The third-order horizontal vorticity is forced by the second-order buoyancy distribution (2.15c) and first-order advection, tilting, and stretching terms.

The most intriguing aspect of the equations for the third-order variables is the generation of third-order vertical vorticity by tilting of the first-order horizontal vorticity by the first-order vertical velocity field (2.15d), a nonlinear process involving only the basic meridional circulation. There is no third-order stretching effect since the first-order vertical vorticity is zero. Equation (2.15d) shows that the tilting term is nonzero in regions where first-order horizontal vorticity vectors cross isolines of first-order vertical velocity. In view of (2.13c), it can be stated equivalently that tilting occurs when isolines of zeroth-order buoyancy cross isolines of the first-order vertical velocity (in the horizontal plane). Using (2.13b) to eliminate vertical velocity in favor of pressure results in another expression for tilting [latter part of (2.15d)]. This latter equation shows that tilting is associated with a nonhydrostatic zeroth-order pressure gradient; that is, only the nonhydrostatic part of the zeroth-order pressure gradient contributes to third-order vertical vorticity generation. The tilting term is maximized for zeroth-order temperature and vertical pressure gradient contours that are perpendicular to each other:

$$\boldsymbol{\nabla}_H\frac{\partial\tilde{\Pi}^0}{\partial z}\perp\boldsymbol{\nabla}_H\tilde{T}^0. \tag{2.16}$$

We note that although this third-order flow is rotational (possesses vertical vorticity), we do not know if it is actually associated with vortices.[1]

In closing this section we note that since the thermal bubble immediately causes an adjustment in the velocity field (creation of a meridional circulation that destroys the initial state of no motion), such an initially resting isolated bubble can never actually be realized in the atmosphere. On the other hand, an initially motionless bubble with controllable geometrical parameters provides a particularly clean model for systematically studying the mechanism of vorticity generation by azimuthal asymmetry. We proceed on the assumption that our idealized model can reproduce the gross features of the more realistic atmospheric thermal bubbles with small but nonzero initial velocity fields.

3. Analytical solutions for thermal bubbles

a. An array of thermal bubbles

Consider an infinite three-dimensional grid or ''checkerboard'' of alternating hot and cold thermal bubbles specified by

$$\tilde{T}^0 = A \sin(kx) \sin(ly) \sin(mz), \tag{3.1}$$

where A is the perturbation temperature amplitude, and k, l, and m are the disturbance wavenumbers in the x, y, and z directions, respectively. With the zeroth-order pressure corresponding to this thermal grid obtained from (2.12b), we find that

$$\frac{\partial \tilde{\Pi}^0}{\partial z} = g\alpha A\left(\frac{m^2}{k^2 + l^2 + m^2}\right) \sin(kx) \sin(ly) \sin(mz). \tag{3.2}$$

Thus the zeroth-order temperature and vertical pressure gradient are proportional to each other. According to (2.13b) they are also proportional to the first-order vertical velocity field. It follows from (2.13c) that the first-order horizontal vorticity vector does not cross isolines of vertical velocity. Thus, the tilting term in (2.15d) vanishes and there is no third-order generation of vertical vorticity, although we cannot rule out higher-order vertical vorticity production. The meridional circulation induced by the array of bubbles inhibits the tilting process, at least as a third-order effect.

b. An isolated ellipsoidal thermal bubble

1) ZEROTH-ORDER THERMODYNAMIC FIELDS

A particularly simple analytical form for an isolated bubble is given by a perturbation pressure of the form

$$\tilde{\Pi}^0 = -g\alpha B z e^{-\chi}, \tag{3.3}$$

where

$$\chi = \frac{x^2}{2L_x^2} + \frac{y^2}{2L_y^2} + \frac{z^2}{2L_z^2}. \tag{3.4}$$

In view of (3.3) and (3.4), isolines of the zeroth-order perturbation pressure (and of the vertical derivative of the zeroth-order perturbation pressure) in any horizontal plane are ellipses with eccentricity $e_p = (1 - L_x^2/L_y^2)^{1/2}$ (where, without loss of generality, we have taken $L_y > L_x$).

Applying (3.3) in (2.12b) and integrating with respect to z yields the zeroth-order perturbation temperature

$$\tilde{T}^0 = B\left[\frac{L_z^2}{L_x^2}\left(\frac{x^2}{L_x^2} - 1\right) + \frac{L_z^2}{L_y^2}\left(\frac{y^2}{L_y^2} - 1\right) + \left(\frac{z^2}{L_z^2} - 1\right)\right]e^{-\chi}. \tag{3.5}$$

A sample contour plot of $\tilde{T}^0$ on the upper-right quadrant of the horizontal plane $z = 0$ through the center of the bubble is presented in Fig. 12a. According to (2.13c) and the fact that the first-order vorticity is purely horizontal, these $\tilde{T}^0$ contours are coincident with first-order vortex lines.

With attention restricted to $B < 0$, the perturbation temperature field corresponds to a central warm bubble surrounded by a slightly cool exterior. The largest temperature perturbation occurs at the origin (0, 0, 0), and B is related to the peak temperature perturbation by

$$B = -\frac{\tilde{T}^0(0, 0, 0)}{1 + L_z^2/L_x^2 + L_z^2/L_y^2}. \tag{3.6}$$

The locus of points $\tilde{T}^0(x, y, z) = 0$ bounding the warm bubble is the ellipsoid

$$\frac{x^2}{L_x^4} + \frac{y^2}{L_y^4} + \frac{z^2}{L_z^4} = \frac{1}{L_x^2} + \frac{1}{L_y^2} + \frac{1}{L_z^2}. \tag{3.7}$$

Thus, in the x–y plane through the bubble center ($z = 0$), the warm bubble is bounded by an ellipse of half-axis lengths $L_x^2(1/L_x^2 + 1/L_y^2 + 1/L_z^2)^{1/2}$ and $L_y^2(1/L_x^2 + 1/L_y^2 + 1/L_z^2)^{1/2}$ in the x and y directions, respectively. The eccentricity of this zero degree perturbation temperature ellipse is $e_{\text{warm}} = (1 - L_x^4/L_y^4)^{1/2}$.

The existence of the weak outer moat of cool air surrounding the central warm bubble is an unavoidable side effect of this analytic model. However, a comparison of numerical simulations initialized with and without the cool exterior (not shown) indicated that the cool air had little affect on the main qualitative results of this study. A numerical simulation (not shown) with the azimuthally asymmetric version of Klemp and Wilhelm-

[1] Although vortices are ubiquitous in nature and easily recognizable, there is, at present, no generally accepted precise mathematical definition of a vortex. Working definitions based on specific kinematic features (e.g., closed streamlines or local concentrations of vorticity) are useful in particular contexts but have limited general utility. The deficiencies of common vortex definitions are discussed in detail by Lugt (1979). Herein we refer to vortex in the layman's sense inasmuch as the pattern to which we refer is eddylike.

son's (1978) thermal bubble also yielded qualitatively similar results. Thus, differences in the specific forms of the bubbles appear to have little bearing on the main qualitative results provided the bubble is isolated and has an ''ellipsoidal-like'' azimuthal asymmetry.

2) First-order meridional circulation

The first-order velocity field is obtained from (2.13a) and (2.13b) as

$$\tilde{\mathbf{v}}_H^1 = -g\alpha Bz\left(\frac{x}{L_x^2}\mathbf{i} + \frac{y}{L_y^2}\mathbf{j}\right)e^{-\chi}, \tag{3.8}$$

$$\tilde{w}^1 = g\alpha B\left[\frac{L_z^2}{L_x^2}\left(\frac{x^2}{L_x^2} - 1\right) + \frac{L_z^2}{L_y^2}\left(\frac{y^2}{L_y^2} - 1\right)\right]e^{-\chi}. \tag{3.9}$$

The peak updraft speed (which occurs at the origin) increases as the vertical aspect ratios L_z/L_x and L_z/L_y increase (narrow bubbles rise faster than wide bubbles), and asymptotically approaches the value $g\alpha\tilde{T}^0(0, 0, 0)$ as $L_z \to \infty$.

Examining (3.9) we see that the locus of points $\tilde{w}^1(x, y, z) = 0$ bounding the updraft region is the elliptical cylinder

$$\frac{x^2}{L_x^4} + \frac{y^2}{L_y^4} = \frac{1}{L_x^2} + \frac{1}{L_y^2}. \tag{3.10}$$

Thus, on any x–y plane, the updraft is an ellipse with half-axis lengths of $L_x^2(1/L_x^2 + 1/L_y^2)^{1/2}$ and $L_y^2(1/L_x^2 + 1/L_y^2)^{1/2}$ in the x and y directions, respectively.

A comparison of the warm bubble and updraft ellipses on the plane $z = 0$ shows that the updraft ellipse is smaller (in both x and y directions) than the warm bubble ellipse. Thus, on the $z = 0$ plane, the warm region of the bubble completely envelopes the updraft as well as part of the surrounding downdraft. However, as the vertical aspect ratios increase, the updraft occupies a larger fraction of the warm bubble (with the isoline of zero vertical velocity approaching the isoline of zero temperature perturbation as $L_z \to \infty$). Despite the relatively smaller size of the updraft, the eccentricities of the updraft and warm bubble ellipses are the same [$e_{\text{up}} = e_{\text{warm}} = (1 - L_x^4/L_y^4)^{1/2}$]. It can be readily shown that the eccentricity of isolines of the perturbation pressure and of the vertical derivative of the perturbation pressure is smaller than the eccentricity of the updraft and warm bubble ellipses: $e_p/e_{\text{warm}} = e_p/e_{\text{up}} = 1/(1 + L_x^2/L_y^2)^{1/2} < 1$. It is in this sense that we say the zeroth-order pressure field (and zeroth-order vertical pressure gradient) is broader than the zeroth-order temperature and first-order vertical velocity fields. We will return to this point in section 4d(4) when we discuss the physical mechanism of vertical vorticity production.

3) Second-order thermodynamic fields

Applying (3.8), (3.9), and (3.5) in (2.14a), yields the second-order temperature as,

$$\begin{aligned}\tilde{T}^2 = {} & g\alpha B^2 L_z^2 z\left(\frac{x^2}{L_x^6} + \frac{y^2}{L_y^6}\right)e^{-2\chi} \\ & + \frac{g\alpha B^2}{2}\left(\frac{1}{L_x^2} + \frac{1}{L_y^2}\right)z\left(1 - \frac{z^2}{L_z^2}\right)e^{-2\chi} \\ & - \frac{g\alpha B^2}{2}L_z^2 z\left(\frac{1}{L_x^2} + \frac{1}{L_y^2} + \frac{2}{L_z^2}\right) \\ & \times \left(\frac{x^2}{L_x^4} + \frac{y^2}{L_y^4} - \frac{1}{L_x^2} - \frac{1}{L_y^2}\right)e^{-2\chi}.\end{aligned} \tag{3.11}$$

A closed-form solution of (2.14b) for the second-order pressure can be obtained by the method of Green's functions, but its form is cumbersome and is not presented.

4) Third-order vorticity distribution

Because of the presence of the second-order pressure in (2.15a) and (2.15b), the analytic form for the third-order velocity field is complicated and not particularly illuminating. However, the third-order vorticity components (2.15c) and (2.15d) can readily be derived since they only require knowledge of the first-order velocity fields and second-order temperature. Our focus now is on the third-order vertical vorticity. Applying (3.3) and (3.5) in (2.15d), we obtain the simple form,

$$\tilde{\zeta}^3 = \frac{2}{3}g^2\alpha^2 B^2\left(1 - \frac{z^2}{L_z^2}\right)\frac{x}{L_x^2}\frac{y}{L_y^2}L_z^2\left(\frac{1}{L_x^2} - \frac{1}{L_y^2}\right)e^{-2\chi}. \tag{3.12}$$

In the axisymmetric case ($L_x = L_y$), the vertical vorticity is zero everywhere. In the nonaxisymmetric case ($L_x \neq L_y$), the vertical vorticity field appears as a four-leaf clover pattern in the horizontal with lobes of alternating positive and negative sign. Sample contours of one ''leaf'' of the $\tilde{\zeta}^3$ pattern in a nonaxisymmetric case can be seen in Fig. 12c. [Figure 12c actually depicts the tilting term, but in view of (2.15d), contours of the tilting term and $\tilde{\zeta}^3$ coincide.]

Primary local extrema in $\tilde{\zeta}^3$ occur at $(x', y', z') = (\pm L_x/\sqrt{2}, \pm L_y/\sqrt{2}, 0)$. Much weaker secondary extrema occur at upper and lower levels of the bubble, at $(x'', y'', z'') = (\pm L_x/\sqrt{2}, \pm L_y/\sqrt{2}, \pm\sqrt{2}L_z)$. The peak magnitude of the vertical vorticity $\tilde{\zeta}^3_{\max} \equiv |\tilde{\zeta}^3(x', y', z')|$ is

$$\tilde{\zeta}^3_{\max} = \frac{1}{3e}g^2\alpha^2 B^2\frac{L_z^2}{L_x L_y}\left|\frac{1}{L_x^2} - \frac{1}{L_y^2}\right|. \tag{3.13}$$

Using (3.6) to eliminate B in favor of the maximum temperature perturbation, (3.13) becomes

$$\tilde{\zeta}^3_{\max} = \frac{1}{3e}g^2\alpha^2\frac{[\tilde{T}^0(0, 0, 0)]^2}{(1 + L_z^2/L_x^2 + L_z^2/L_y^2)^2}\frac{L_z^2}{L_x L_y}\left|\frac{1}{L_x^2} - \frac{1}{L_y^2}\right|. \tag{3.14}$$

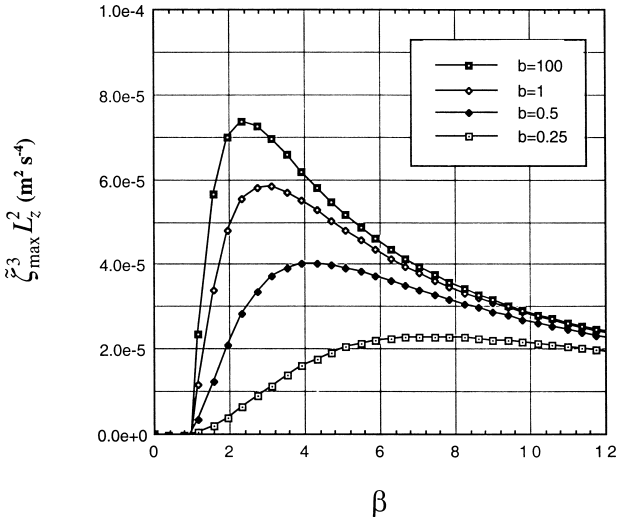

FIG. 1. Third-order domain maximum vertical vorticity (times L_z^2) as a function of horizontal aspect ratio β ($=L_y/L_x$), for vertical aspect ratios $b = 100$, 1, 0.5, and 0.25.

The magnitude of the maximum vertical vorticity is directly proportional to the square of the temperature perturbation. However, the dependence of the vorticity on the bubble dimensions is more complicated. For a thermal bubble of fixed vertical thickness (L_z = constant), the maximum vertical vorticity is proportional to

$$\tilde{\zeta}^3_{\max} \propto \frac{ab|a^2 - b^2|}{(1 + a^2 + b^2)^2}, \tag{3.15}$$

where $a \equiv L_z/L_x$ and $b \equiv L_z/L_y$ are the vertical aspect ratios. The vertical vorticity is zero if $a = b$ (axisymmetric bubble) or if a or b are zero. In the latter case a horizontal length scale becomes infinite and the problem becomes two-dimensional (slab symmetric).

It can be shown that without further restrictions on the bubble geometry, there are no local extrema of $\tilde{\zeta}^3_{\max}$ in a–b parameter space. However, we can find a local extrema in a restricted sense if we regard b as fixed and let a vary according to $a = \beta b$, where β ($=a/b = L_y/L_x$) is the horizontal aspect ratio. Without further loss of generality, we take $\beta > 1$, so $L_y > L_x$. The peak vertical vorticity is then proportional to

$$\tilde{\zeta}^3_{\max} \propto \frac{b^4\beta(\beta^2 - 1)}{[1 + b^2(1 + \beta^2)]^2}. \tag{3.16}$$

This relationship is illustrated in Fig. 1. Note that for slightly azimuthally asymmetric bubbles (β slightly bigger than 1) with vertical aspect ratios ranging between $b = 1$ ($L_z = L_y$) and $b = 100$ ($L_z \gg L_y$)(a range within which thermals in the planetary boundary layer typically fall), vertical vorticity generation increases rapidly with β. The horizontal aspect ratio $\beta_{\max}$ that maximizes the vertical vorticity is determined by the condition $\partial\tilde{\zeta}^3_{\max}/\partial\beta = 0$ as

$$\beta_{\max} = \left\{\left(3 + \frac{3}{2b^2}\right) \pm \left[\left(3 + \frac{3}{2b^2}\right)^2 - \left(1 + \frac{1}{b^2}\right)\right]^{1/2}\right\}^{1/2}. \tag{3.17}$$

We consider the limiting cases of (3.17) for b small and large. For $b \ll 1$ (bubble with a very wide profile in the y–z plane), $\beta_{\max}$ is approximately

$$\beta_{\max} \approx \frac{\sqrt{3}}{b} \approx \frac{1.732}{b}, \tag{3.18}$$

and $a \approx 1.732$. Thus, the horizontal aspect ratio $\beta_{\max}$ that maximizes the vorticity is very large ($L_y \gg L_x$) and the bubble profile in the x–z plane is fairly narrow ($L_z = 1.732\, L_x$). For $b \gg 1$ (narrow bubble in the y–z plane), $\beta_{\max}$ is approximately

$$\beta_{\max} \approx (3 + 2\sqrt{2})^{1/2} \approx 2.414, \tag{3.19}$$

and so $a \approx 2.414\, b$. Thus, the horizontal aspect ratio $\beta_{\max}$ that maximizes the vertical vorticity is approximately 2.414; that is, $L_y = 2.414\, L_x$.

It is important to remember that our discussion of bubble shapes that maximize vertical vorticity production and use of (3.15)–(3.19) apply to a family of bubbles of constant vertical thickness L_z. Separate analyses are required for different restrictions, for example, for the family of bubbles of constant volume or constant horizontal cross-sectional area.

Although the third-order flow is rotational (vertical vorticity is present), we do not know if actual vortices are present. By inspection we find that a third-order horizontal wind field consistent with (3.12) is

$$\tilde{\mathbf{v}}^3_H = \frac{1}{6}g^2\alpha^2B^2\left(1 - \frac{z^2}{L_z^2}\right)\left(\frac{x}{L_x^2}\mathbf{i} - \frac{y}{L_y^2}\mathbf{j}\right)L_z^2\left(\frac{1}{L_x^2} - \frac{1}{L_y^2}\right)e^{-2x}. \tag{3.20}$$

Since $u \propto xe^{-2x}$ and $v \propto -ye^{-2x}$, this flow is similar to classical stagnation point flow (an irrotational flow with $u \propto x$ and $v \propto -y$), but with regions of inflow and outflow that are sheared and jetlike (rotational) due to the extra factor of e^{-2x}. Thus, we are tempted to say that the third-order flow, although rotational, is not characterized by vortices. The numerical simulations conducted in the next section also suggest that vortex production is a higher-than-third-order effect, at least for the cases considered. However, one should keep in mind that (3.20) is just the rotational component of the horizontal wind (not the complete horizontal wind), and we cannot exclude the possibility that for some thermal bubbles the addition of an irrotational flow component would manifest a closed vortex circulation.[2]

[2] As a simple example, consider a Rankine vortex with peak tangential wind U embedded in a uniform easterly current $-U$. Since the easterly current masks the vortex (we do not readily perceive the embedded vortex) we would likely characterize the flow as rotational but nonvortical. However, superposition of a uniform (irrotational) westerly current U on this rotational nonvortical flow would undo the effect of the easterly current and reveal the vortex.

TABLE 1. Summary of numerical experiment parameters.

	CNTRL	EXPT1	EXPT2	EXPT3	EXPT4	EXPT5	EXPT6
Geometry							
x–y	Circle	Ellipse	Ellipse	Ellipse	Ellipse	Ellipse	Ellipse
x–z	Circle	Narrow ellipse	Narrow ellipse	Narrow ellipse	Circle	Wide ellipse	Wide ellipse
y–z	Circle	Circle	Narrow ellipse	Wide ellipse	Wide ellipse	Wide ellipse	Wide ellipse
L_x (m)	64.24	26.84	20.84	20.84	26.84	20.84	20.84
L_y (m)	64.24	64.24	49.88	64.24	64.24	49.88	49.88
L_z (m)	64.24	64.24	64.24	49.88	26.84	19.23	19.23
$a = L_z/L_x$	1.000	2.393	3.083	2.393	1.000	0.923	0.923
$b = L_z/L_y$	1.000	1.000	0.288	0.777	0.418	0.386	0.386
$\beta = a/b$	1.000	2.393	2.393	3.083	2.393	2.393	2.393
$T(0, 0, 0)$ (K)	1.5	1.5	1.5	1.5	1.5	1.5	3.0
B	−0.5000	−0.1940	−0.1233	−0.2045	−0.6897	−0.7499	−1.4999

4. Numerical simulations

a. Numerical model

The early time analytic theory of the previous sections is complemented with numerical model simulations. Our research tool is Kanak's System for Atmospheric Simulation (KANSAS), a three-dimensional, nonhydrostatic, compressible, dry convective numerical model patterned on the work of Chorin (1967). The governing equations are cast on a Cartesian Arakawa C grid. Velocity and pressure variables are integrated with a second-order, quadratic-conserving spatial discretization technique known as the box scheme (Kurihara and Holloway 1967), and the centered-in-time leapfrog method. The thermodynamic variable (potential temperature) is integrated using a sixth-order, flux conservative Crowley scheme (Tremback et al. 1987) with a forward time step. A monotonic flux corrector (Leonard 1991), a high-order operator that guarantees monotonicity, is also used in the potential temperature calculation. A time filter (Asselin 1972) is applied to the velocity variables to prevent solution decoupling. To improve computational efficiency, a time-splitting scheme (Klemp and Wilhelmson 1978) is used to integrate terms supporting sound waves with small time steps, and terms supporting the slower advective process with larger time steps. Lateral boundary conditions are open/radiative (Klemp and Wilhelmson 1978), whereas, the lower and upper boundary conditions are rigid and free-slip. No explicit physical or computational diffusion processes are incorporated. Further details of this numerical model can be found in Kanak et al. (2000).

b. Experimental design

A substantial computational saving can be obtained by exploiting the symmetry of the problem. Since there is no environmental wind, the bubble remains symmetric about the x and y coordinate axes, and it suffices to model the flow on any one quadrant (the flow on the

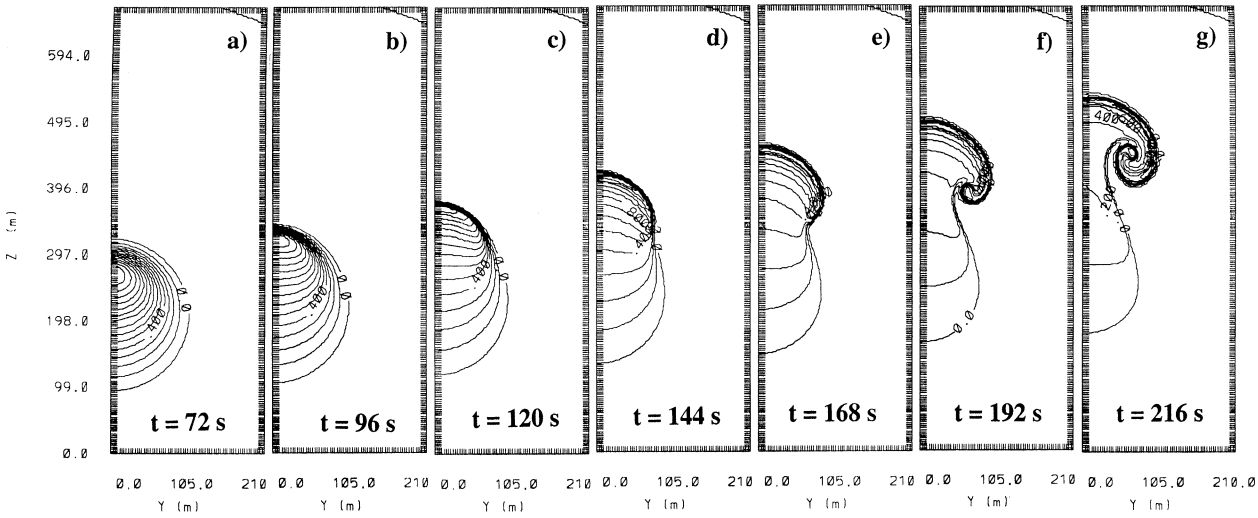

FIG. 2. The *y–z* cross section of perturbation potential temperature for the CNTRL simulation through the center of the bubble ($x = 0$ m) at various times: (a) $t = 72$ s, (b) $t = 96$ s, (c) $t = 120$ s, (d) $t = 144$ s, (e) $t = 168$ s, (f) $t = 192$ s, and (g) $t = 216$ s. Contour interval is 0.1 K.

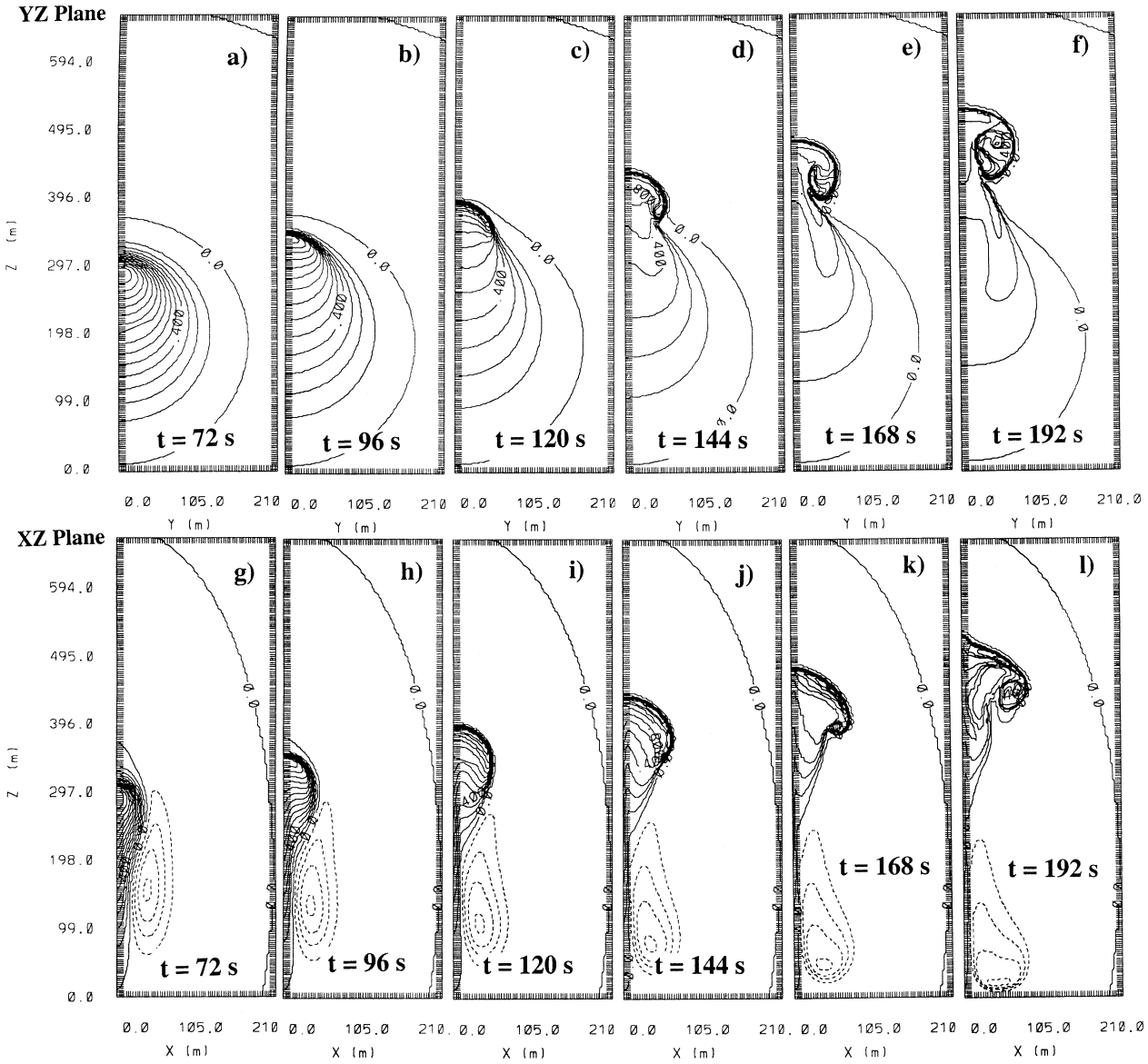

FIG. 3. Cross sections of perturbation potential temperature for EXPT1 through the center of the bubble at the same times as Fig. 2. (a)–(f) The y–z cross sections. (g)–(l) The x–z cross sections. Contour interval is 0.1 K.

full domain can be obtained by appropriate reflections of the quadrant solution). In the following, we simulate the flow on the upper right quadrant ($x \geq 0$, $y \geq 0$).

Our single-quadrant simulations employ $77 \times 77 \times 224$ grid points in the x, y, and z directions, respectively, with a resolution of $\Delta x = \Delta y = \Delta z = 3$ m. The large time step is set at $\Delta t = 0.06$ s, and the small time step is set at $\Delta t = 0.001\,45$ s. The base state potential temperature is set to 300 K. The model surface pressure is set to 1000 mb.

The initial condition is prescribed by (3.5) but applied to the perturbation potential temperature rather than to the perturbation temperature (the difference between these two variables being very small given the relatively small size and small vertical displacements of the bubble). The bubble initially is centered at $x = 0$ m, $y = 0$ m, $z = 189$ m. Seven simulations were performed. The first simulation (CNTRL) was a spherical bubble control run with $L_x = L_y = L_z = 64.24$ m, and an initial perturbation potential temperature amplitude of 1.5 K. Simulations EXPT1–EXPT5 focussed on the sensitivity of the bubble evolution to variations in horizontal and vertical aspect ratios. Equation (3.6) was used to determine the coefficient B for each simulation (again, with perturbation potential temperature used in place of perturbation temperature). The bubble in the last simulation, EXPT6, had an initial perturbation amplitude of 3.0 K—twice that of the bubbles in the other sim-

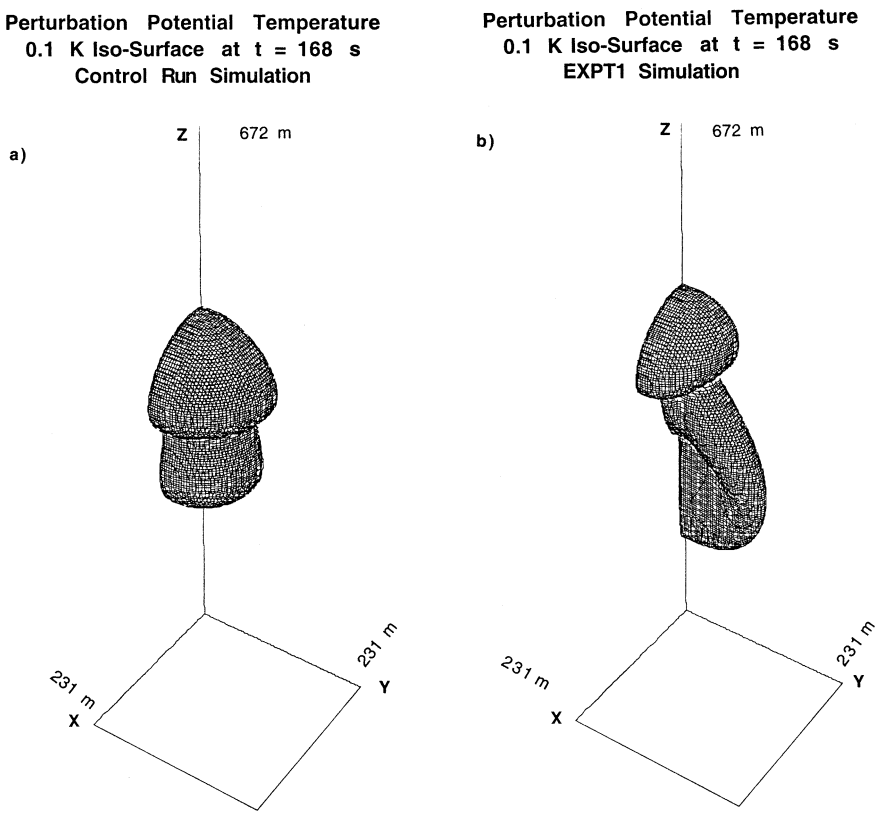

FIG. 4. Isosurface of the 0.1-K perturbation potential temperature at $t = 168$ s for the (a) CNTRL and (b) EXPT1 simulations. One quadrant of the domain is depicted.

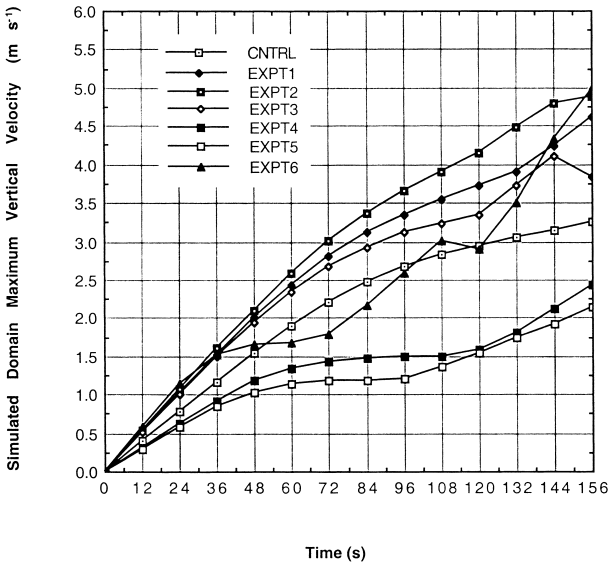

FIG. 5. Time series of domain maximum vertical velocity (m s^{-1}) for each numerical experiment (time sampling interval is 12 s).

ulations. The simulation parameters are summarized in Table 1.

c. Control run

Figure 2 displays a vertical cross section (y–z plane) of the evolving perturbation potential temperature field for the initially spherical bubble control run (CNTRL). The fields are shown at 24-s intervals beginning at $t =$ 72 s. As in previous studies of isolated convection (e.g., Woodward 1959), the bubble rises and produces a horizontally convergent inflow beneath the region of maximum vertical velocity, and a horizontally divergent outflow region near the top of the bubble. This meridional circulation is associated with strong toroidal (ringlike) vorticity in the horizontal.

In the absence of explicit physical or computational diffusion, the peak value of the perturbation potential temperature should remain at 1.5 K. However, since the numerical schemes have a small amount of implicit diffusion, the simulated peak value will generally be less than the theoretical value. The peak value in the control run stays close to 1.5 K for times up to 120 s, but then begins to decline as the temperature gradient along the leading edge of the bubble becomes large. At 120 s the peak value is 1.47 K. From 144 s until the termination

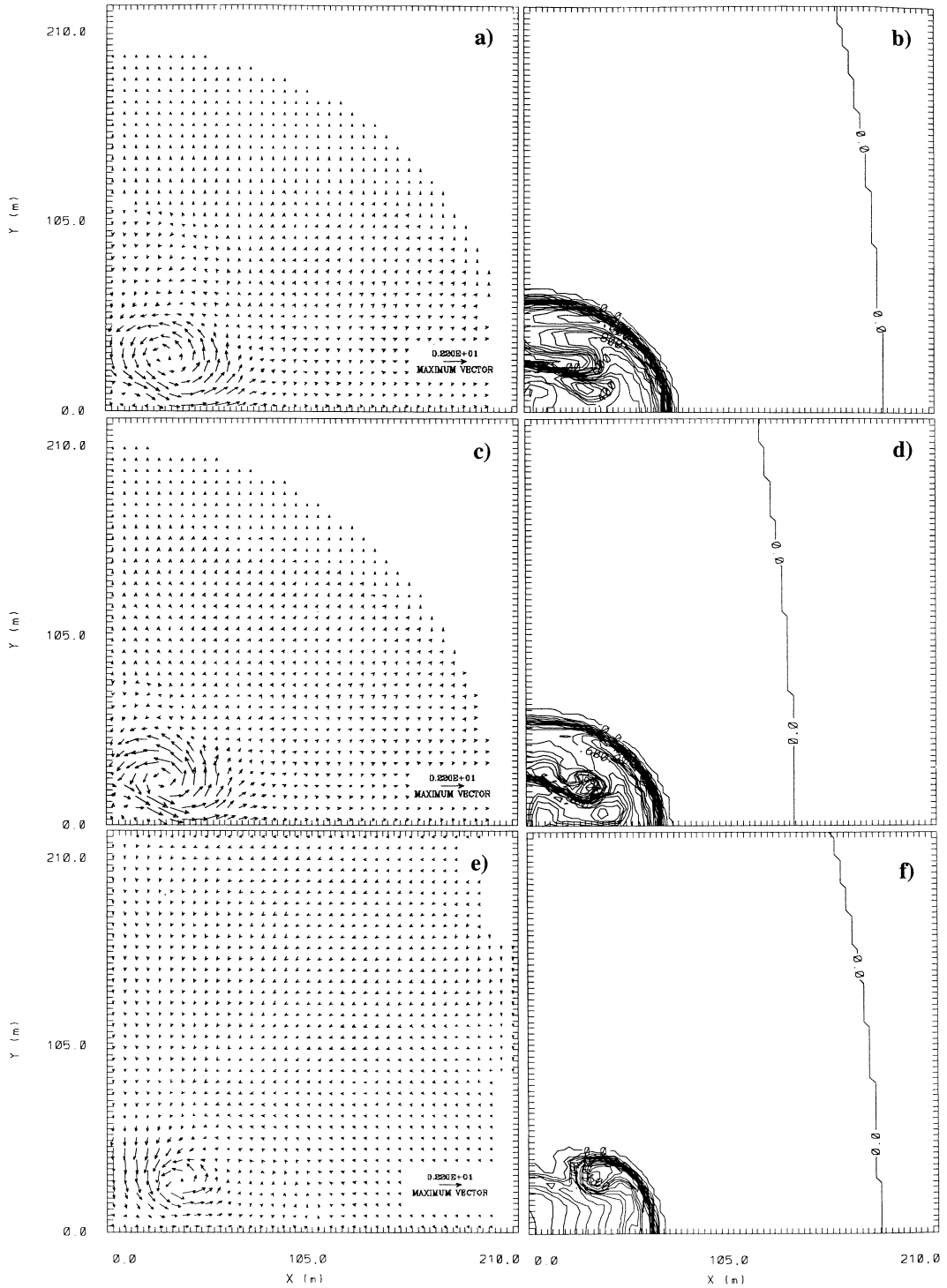

FIG. 6. Horizontal cross sections of selected fields at $t = 168$ s for (a)–(b) EXPT1, (c)–(d) EXPT3, and (e)–(f) EXPT4. (a) Horizontal velocity vectors at $z = 418.5$ m. (b) Perturbation potential temperature contours at $z = 418.5$ m. Contour interval is 0.05 K. (c) Horizontal velocity vectors at $z = 388.5$ m. (d) Perturbation potential temperature contours at $z = 388.5$ m. Contour interval is 0.05 K. (e) Horizontal velocity vectors at $z = 289.5$ m. (f) Perturbation potential temperature contours at $z = 289.5$ m. Contour interval is 0.05 K.

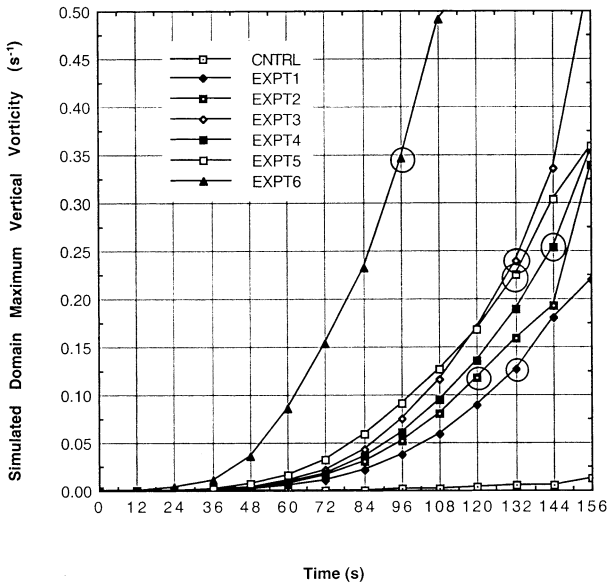

FIG. 7. Time series of domain maximum vertical vorticity for each numerical experiment (time sampling interval is 12 s).

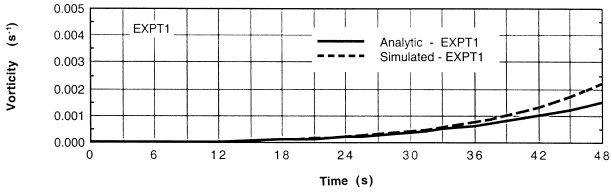

FIG. 8. Time series of EXPT1 domain maximum vertical vorticity compared with the corresponding analytic maximum value (time sampling interval is 1.5 s).

of the simulation at 216 s, the peak value decreases from 1.35 to 0.93 K. A similar decline in peak bubble temperature is found in the ellipsoidal bubble simulations.

The equations for the third-order variables predict zero third-order vertical vorticity values for the control run (more generally, no vertical vorticity should ever be generated for this flow). In agreement with the analytical solution, the control simulation produced no physically meaningful values of vertical vorticity. However, weak vertical vorticity values several orders of magnitude less than in any of the other simulations were present in the form of gridscale noise (not shown). We attribute these spurious values to the numerical discretization errors inherent in the numerical integration of the equations.

d. Ellipsoidal bubble simulations

1) POTENTIAL TEMPERATURE

As an illustrative example of the common qualitative behavior of ellipsoidal thermal bubbles, we focus on the EXPT1 simulation. The initial bubble in this simulation is wider in the *y* direction than the *x* direction by a factor of almost 2.5 (L_y = 64.24 m, L_x = 26.84 m), with a vertical length scale L_z equal to L_y. Accordingly, we say that this bubble is narrow in the *x*–*z* plane, and circular in the *y*–*z* plane. The evolution of the potential temperature field in a *y*–*z* cross section through the bubble center ($x = 0$) is shown in Figs. 3a–f and in an *x*–*z* cross section through the bubble center ($y = 0$) in Figs. 3g–l. A comparison of Figs. 3a–f (EXPT1) with Figs. 2a–f (CNTRL), shows that the EXPT1 thermal rises faster and develops its characteristic ''mushroom shape'' sooner than in the CNTRL run. In general, the narrower bubbles (EXPT1–EXPT3) rise more rapidly than the wider bubbles (EXPT4, EXPT5), a result consistent with the discussion of the first-order vertical velocity field in section 3b(2) and the results of previous studies (e.g., the appendix of Das 1979). (EXPT3 is a special case where the initial bubble is narrow in the *x*–*z* plane and wide in the *y*–*z* plane, and exhibits behavior that is intermediate to the other simulations.)

Figures 2 and 3 also reveal that although both bubbles have the same initial radius in the *y* direction, the subsequent expansion of the EXPT1 bubble in the *y* direction is significantly inhibited compared to the expansion of the CNTRL bubble. The expansion of the EXPT1 bubble in the *y* direction is also stunted compared to its growth in the *x* direction. These features are particularly evident in the three-dimensional view of the 0.1-K perturbation potential temperature isosurface at $t = 168$ s (Fig. 4). Interestingly, the isosurface for the EXPT1 simulation (Fig. 4b) reveals that the bubble ellipticity reverses with height: at low levels the bubble is elongated in the *y* direction (as in the initial condition), but at upper levels (e.g., in the cap) the bubble is elongated in the *x* direction. This reversal of eccentricity is associated with a sharp indention of the 0.1-K isosurface. As we will see, this unusual structure is associated with vertical vortices induced by the azimuthal asymmetry of the thermal field.

2) MAXIMUM UPDRAFT SPEEDS

The time series of the domain maximum vertical velocity for each simulation is shown in Fig. 5. The CNTRL updraft speed is in the middle of the simulation range, with narrower bubbles (EXPT1–EXPT3) having greater vertical velocities than the wider bubbles (EXPT4 and EXPT5). This ordering of the magnitudes of the peak vertical velocities is consistent with the first-order theory of section 3b(2) throughout the simulation period (although the first-order theory is strictly valid only for the early stages of the simulation, where w varies linearly with time).

3) VERTICAL VORTICITY AND VERTICAL VORTICES

The most intriguing aspect of these results is the formation of vertical vortices in the ellipsoidal bubble runs. Examples of vortices from three simulations at a com-

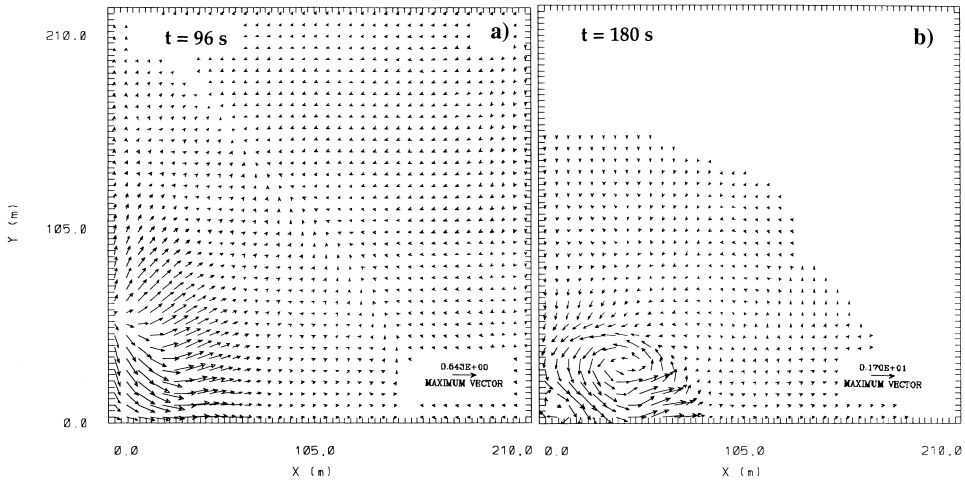

FIG. 9. Horizontal cross sections of horizontal velocity vectors for EXPT1 at (a) $t = 96$ s and $z = 310.5$ m, and (b) $t = 180$ s and $z = 430.5$ m.

mon time, $t = 168$ s, are presented in Fig. 6. Figures 6a–b depict the horizontal velocity vectors and perturbation potential temperature contours in the x–y plane at the height $z = 418.5$ m for EXPT1. Figures 6c–d depict the same fields, but for EXPT3 at $z = 388.5$ m. Figures 6d–e depict the same fields, but for EXPT4 at $z = 289.5$ m. These heights were chosen because they contained the most pronounced vertical vortices. These heights are also within a few levels of the domain maximum vertical vorticity values.

In these and in the other simulations, the sense of the vortex circulations is such that the advection of the temperature field reduces (and eventually reverses) the sense of the thermal bubble eccentricity. The potential temperature perturbation fields shown in Figs. 6b,d, and f, all reflect the reversed or reduced eccentricity of the thermal field associated with the vortices. These figures (especially Fig. 6d) also show a pronounced ''wrapping up'' of the perturbation temperature contours.

A time series of the domain maximum vertical vorticity for each simulation is shown in Fig. 7. The open circles on each curve correspond to the approximate (subjectively determined) time at which a vortex circulation was first evident in the simulation. According to (3.14), the wide bubbles should have the greatest values of vertical vorticity, and the narrow bubbles should have the lowest values. The results depicted in Fig. 7 are consistent with this prediction. The development of a mushroom-shaped cap in the perturbation temperature field, the vortex formation, and the subsequent wrapping up of the perturbation temperature contours occurred somewhat earlier in the narrower bubble simulations than in the wider bubble simulations, even though the wider bubbles eventually developed

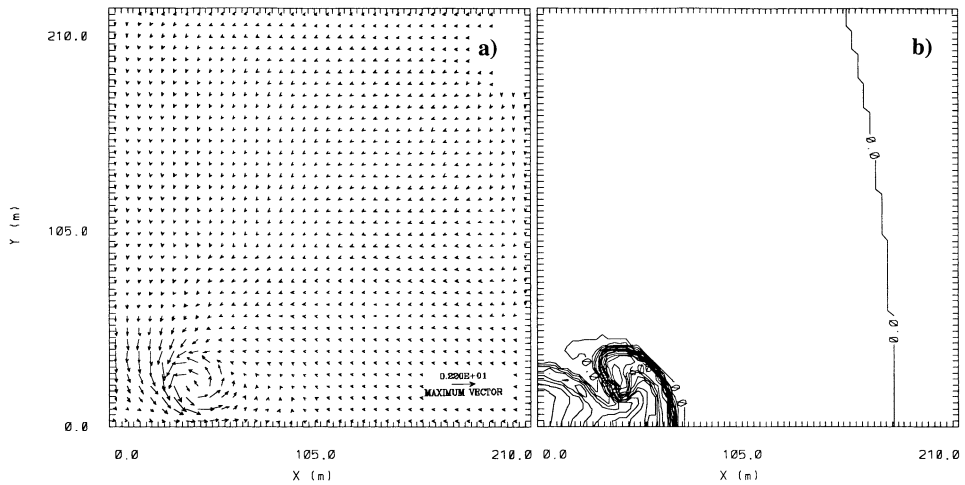

FIG. 10. Horizontal cross sections for EXPT4 at $t = 180$ s and $z = 292.5$ m. (a) Horizontal velocity vectors and (b) perturbation potential temperature. Contour interval is 0.05 K.

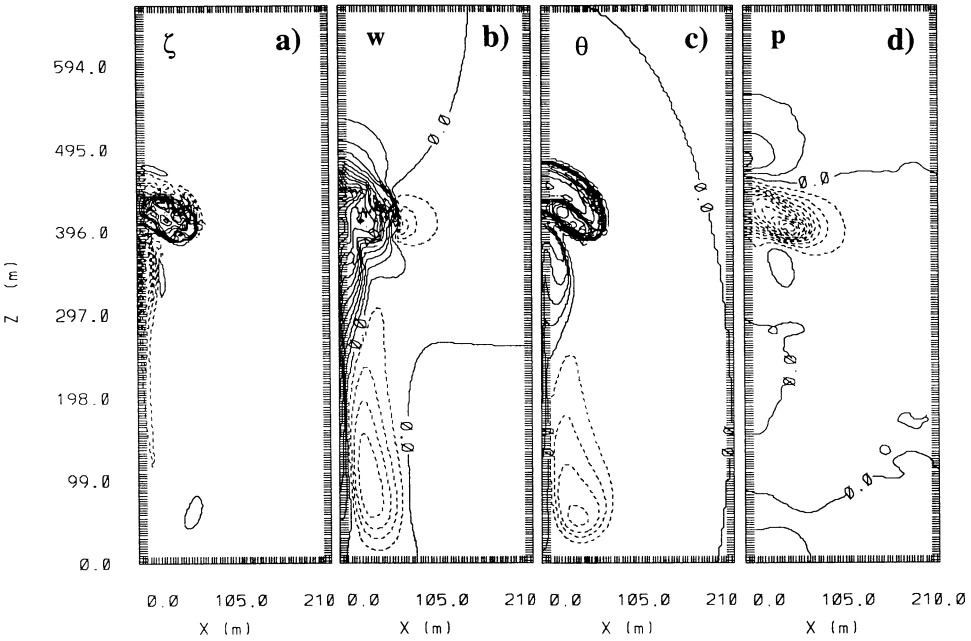

FIG. 11. Vertical cross section of selected fields for EXPT1 at $t = 168$ s and $y = 25.5$ m. (a) Vertical vorticity. Contour interval is 0.02 s^{-1}. (b) Vertical velocity. Contour interval is 0.3 m s^{-1}. (c) Perturbation potential temperature. Contour interval is 0.09 K. (d) Perturbation pressure. Contour interval is 0.5 Pa.

greater values of vertical vorticity. Note that EXPT6 (which has twice the initial thermal perturbation amplitude of the other simulations) has maximum vertical vorticity values much larger than in all the other simulations.

In Fig. 8 the theoretical value of maximum third-order vertical vorticity (3.14) (multiplied by t^3) is compared to the simulated maximum value in the EXPT1 run. The predicted solution agrees well with the simulated domain maximum vertical vorticity for early times (when the theory is valid). Similarly good agreements with the theoretical curves were obtained for all other simulations, although the curves tended to diverge earlier for the bubbles with the greatest vertical velocities.

Horizontal wind vectors for EXPT1 are shown in Fig. 9 for two times, $t = 96$ s and $t = 180$ s, at the heights $z = 310.5$ and 430.5 m, respectively. Although vorticity is present at $t = 96$ s, a vortex does not form until $t > 120$ s. The flow represented in Fig. 9a is qualitatively similar to the analytical solution for the rotational part of the wind (3.20) in that it resembles a stagnation point-type flow, at least for $y < 50$ m. At $t = 180$ s (Fig. 9b), a vortex is well established. A small counterrotating subvortex near the bubble center is also evident at this time.

The wrapping up of the thermal field is particularly evident in the wide bubble of EXPT4, which appears to be in the process of splitting at $t = 180$ s (Fig. 10). Since each panel represents a single quadrant, the full bubble appearance after such a split would be a central cell and two lateral cells on either side in the x direction. Such a result might be counterintuitive (the initial bubble geometry is elongated along the y direction) until one considers the sense of the vortex circulations. However, after $t = 180$ s the bubble geometry becomes increasingly complicated and noisy, and the grid resolution may become inadequate. Accordingly, we postpone further comments on this possible splitting behavior until a later study, when we plan to conduct higher-resolution and larger domain tests.

The vertical structure (x–z cross section), taken through the center of the primary EXPT1 vortex at $t = 168$ s is shown in Fig. 11. The vertical vorticity associated with this vortex is shaped like a canopy (Fig. 11a) overlying a narrow and vertically extensive core of weak vorticity of opposite sense, which is eventually associated with the small inner subvortex depicted in Fig. 9b. The vertical velocity field (Fig. 11b) shows that the primary vortex resides largely within rising motion. The perturbation pressure (Fig. 11d) shows that the vortex is associated with low pressure, as expected.

4) MECHANISM OF VERTICAL VORTICITY PRODUCTION

As discussed in section 2c, the lowest-order (third-order) vertical vorticity is produced by the tilting of the first-order horizontal vorticity into the vertical by the first-order vertical velocity. This is an interaction between two features that characterize the basic meridional circulation: the convective updraft and the baroclinically generated toroidal (ring) vorticity. We saw that this tilting process had several equivalent descriptions involving, for example, the cross product between horizontal gradients of first-order vertical velocity and zeroth-order

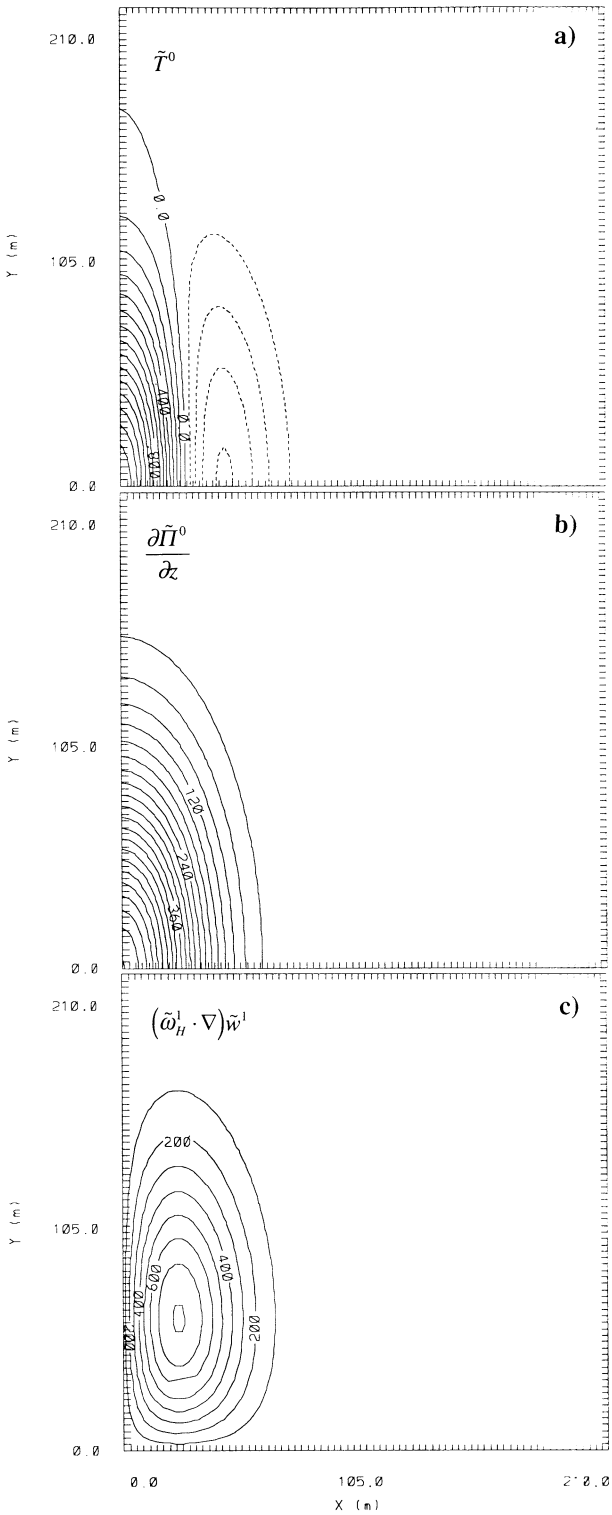

FIG. 12. Horizontal cross sections of analytic fields through center of bubble ($z = 0$) determined with EXPT1 input parameters. (a) Zeroth-order perturbation potential temperature from (3.5). Contour interval is 0.1 K. (b) Vertical derivative of zeroth-order perturbation pressure (divided by density) from (3.3). Contour interval is 0.003 $m^2\ s^{-2}$. Field scaled by 1.0×10^5. (c) Third-order vertical vorticity from (3.12). Contour interval is $1.0 \times 10^{-7}\ s^{-4}$. Field scaled by 1.0×10^{10}.

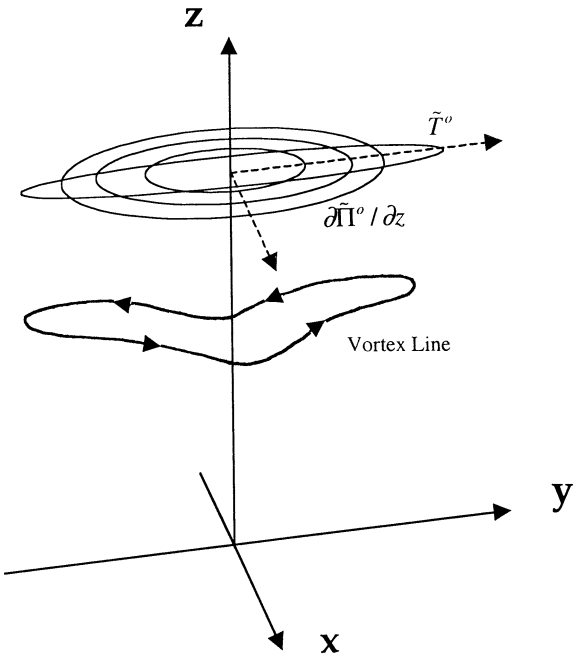

FIG. 13. Schematic diagram illustrating the generation of vertical vorticity in ellipsoidal thermal bubbles. See text for details.

temperature, and the cross product between horizontal gradients of the zeroth-order vertical perturbation pressure gradient and zeroth-order temperature. However, as we will now see, the skewness (crossing angle) between the first-order vertical velocity and zeroth-order temperature isolines can be very small.

Making use of (2.13b) and (3.3)–(3.5), we find that the ratio of the buoyancy force to the vertical pressure gradient force at the center of the ellipsoidal bubble is

$$\left| \frac{g\alpha \tilde{T}(0,\,0,\,0)}{\dfrac{\partial \tilde{\Pi}^0}{\partial z}(0,\,0,\,0)} \right| = 1 + \frac{L_z^2}{L_x^2} + \frac{L_z^2}{L_y^2}. \tag{4.1}$$

Hence, if the bubble is ''narrow'' (one or both of the vertical aspect ratios is greater than one), then the first-order vertical velocity field is dominated by the buoyancy force rather than by the vertical pressure gradient force. Since the vertical velocity field is then mostly proportional to the temperature field, the crossing angle between isolines of vertical velocity and temperature is very small. Consistent with this result, we found that the skewness between isolines of the vertical velocity and potential temperature fields in the region of the maximum tilting were almost imperceptible during the early part of the EXPT1 bubble simulation (not shown). On the other hand, isolines of vertical perturbation pressure gradient and perturbation temperature were much more skewed with respect to each other. Depicted in Fig. 12 are horizontal cross sections through the center of the bubble of three fields determined analytically with EXPT1 input parameters: the zeroth-order perturbation

temperature $\tilde{T}^0$, the vertical derivative of the zeroth-order perturbation pressure $\partial\tilde{\Pi}^0/\partial z$, and the tilting term $(\tilde{\boldsymbol{\omega}}_H^1 \cdot \boldsymbol{\nabla})\tilde{w}^1$. [We remind the reader that contours of $\tilde{T}^0$ coincide with first-order vortex lines through (2.13c), and that contours of the tilting term $(\tilde{\boldsymbol{\omega}}_H^1 \cdot \boldsymbol{\nabla})\tilde{w}^1$ coincide with contours of the third-order vertical vorticity $\tilde{\zeta}^3$ through (2.15d).] Consistent with previous studies of thermal convection (e.g., Das 1979), the positive value of $\partial\tilde{\Pi}^0/\partial z$ indicates that the perturbation pressure gradient force is downward, that is, opposing the buoyancy force. A large skewness between the $\tilde{T}^0$ and $\partial\tilde{\Pi}^0/\partial z$ fields is evident in the region of greatest tilting.

A conceptual model for the early-time generation of vertical vorticity in an elliptical thermal bubble is sketched in Fig. 13. The narrow ellipse at the top of the figure represents an isotherm in the central plane of the bubble. This narrow ellipse is also a vortex line since the vorticity is tangent to the temperature contours at early times. This isotherm is intersected by several broader ellipses representing isolines of the downward-directed vertical perturbation pressure gradient force. The pressure gradient force pushes the isotherm/vortex line downward in a broad central region, distorting its originally planar orientation. Upward- and downward-directed arrows on this vortex line indicate regions where positive (or negative) vertical vorticity are now present.

5. Summary and future work

This study is an analytical and numerical investigation of the early time behavior of a prototypical natural convective flow, the dry thermal bubble, with a novel focus on the impact of asymmetrical bubble geometry (ellipticity in both horizontal and vertical cross sections). For simplicity, we consider the simplest possible scenario of a single bubble rising in an unstratified environment without an ambient wind. Experiments are performed for several combinations of horizontal and vertical aspect ratios.

Since the vertical vorticity in this study is initially zero and there is no environmental wind shear, vertical vorticity can only arise from the tilting of horizontal baroclinically generated vorticity into the vertical. The asymmetrical nature of the bubble allows the tilting process to operate. A perturbation analysis (Taylor series expansion in time) shows that the vertical vorticity first appears as a third-order effect, in a pattern resembling a four-leaf clover. The initial production of vertical vorticity by the tilting mechanism has a straightforward explanation. Since the downward-directed perturbation pressure gradient force is broader than the narrow perturbation temperature field (and associated narrow elliptical vortex line), it acts to broadly depress the elliptical vortex line downward in the central part of the bubble (Fig. 13). The distorted vortex line is then associated with positive and negative components of vertical vorticity.

The numerical simulations show that the rotational flow first appears as a sheared stagnation point-type flow that evolves into four vortices (one primary vortex per quadrant of the bubble) that fill the bubble. Later in the simulations, counter-rotating inner subvortices of considerable vertical extent form near the center of the bubble.

The primary vortex circulations wrap up the temperature contours and also reduce the azimuthal ellipticity of the bubble temperature field. Eventually the eccentricity reverses sense; that is, the bubble becomes elongated in the direction perpendicular to its original major axis. At even later stages of some of the simulations, the bubble appears to be on the verge of splitting, although the grid resolution may not adequately capture this process.

Further experiments with isolated ellipsoidal bubbles are planned. We will first revisit the possible splitting behavior of the bubbles with higher-resolution numerical simulations conducted in a larger domain and for a longer duration than was originally possible. Longer duration experiments with diffusion and with random noise imposed in the initial condition will allow us to assess the significance of the asymmetry-induced vortices against a more realistic backdrop of interface instability and turbulence. In particular, we can determine whether asymmetric thermal bubbles eventually become self-similar like their axisymmetric counterparts. We will then broaden the experimental framework to include continuous density stratification, inversions, wind shear, and latent heat release. We anticipate that when buoyant air rises or neutral or stable air is forced to rise in a unidirectionally sheared environment, a pair of positive and negative vertical vorticity lobes will be generated by the tilting process (e.g., Rotunno 1981; Wilhelmson and Klemp 1978). We also anticipate that vertical displacements in a stratified environment will generate gravity waves that might interact with the thermal. Latent heat release in moist thermals and evaporation in compensating downdrafts can accentuate horizontal temperature gradients that generate horizontal vorticity baroclinically. The impact of these additional processes on the asymmetry-induced tilting process and on vortex evolution will be investigated.

Acknowledgments. The authors are grateful to the anonymous referees for their suggestions and constructive criticisms, and to Jerry M. Straka, Doug Lilly, and Evgeni Fedorovich for helpful discussions of this work. The numerical simulations were performed on the Environmental Computing Application System (ECAS) Cray J90 at the University of Oklahoma. The ECAS is supported by the University of Oklahoma and the National Science Foundation (NSF) under Grant EAR95-12145. The first author was supported by the Center for Analysis and Prediction of Storms (CAPS) under NSF Grant ATM91-20009. The second author was supported by NSF Grant ATM-9727150 and by the Cooperative Institute for Mesoscale Meteorological Studies/National Oceanic and Atmospheric Administration (CIMMS/NOAA) under NSF Grant NA117RJ11227.

REFERENCES

Adem, J., 1956: A series solution for the barotropic vorticity equation and its application in the study of atmospheric vortices. *Tellus,* **8,** 364–372.

Asselin, R., 1972: Frequency filter for time integration. *Mon. Wea. Rev.,* **100,** 487–490.

Batchelor, G. K., 1954: Heat convection and buoyancy effects in fluids. *Quart. J. Roy. Meteor. Soc.,* **80,** 339–358.

Briggs, G. A., 1975: Plume rise from multiple sources. *Cooling Tower Environment,* Technical Information Center, 161–179.

Byers, H. R., and R. R. Braham, 1949: *The Thunderstorm.* U.S. Government Printing Office, 287 pp.

Chorin, A. J., 1967: A numerical method for solving incompressible flow problems. *J. Comput. Phys.,* **2,** 12–16.

Das, P., 1979: A non-Archimedean approach to the equations of convection dynamics. *J. Atmos. Sci.,* **36,** 2183–2190.

Emanuel, K. A., 1994: *Atmospheric Convection.* Oxford University Press, 580 pp.

Grabowski, W. W., and T. L. Clark, 1991: Cloud-environment interface instability: Rising thermal calculations in two spatial dimensions. *J. Atmos. Sci.,* **48,** 527–546.

——, and ——, 1993a: Cloud-environment interface instability. Part II: Extension to three spatial dimensions. *J. Atmos. Sci.,* **50,** 555–573.

——, and ——, 1993b: Cloud-environment interface instability. Part III: Direct influence of environmental shear. *J. Atmos. Sci.,* **50,** 3821–3828.

Houze, R. A., 1993: *Cloud Dynamics.* International Geophysics Series, Vol. 53, Academic Press, 573 pp.

Kanak, K. M., D. K. Lilly, and J. T. Snow, 2000: The formation of vertical vortices in the convective boundary layer. *Quart. J. Roy. Meteor. Soc.,* **126A,** 2789–2810.

Klemp, J. B., and R. B. Wilhelmson, 1978: The simulation of three-dimensional convective storm dynamics. *J. Atmos. Sci.,* **35,** 1070–1096.

Kogan, Y. L., and A. Shapiro, 1996: The simulation of a convective cloud in a 3D model with explicit microphysics. Part II: Dynamical and microphysical aspects of cloud merger. *J. Atmos. Sci.,* **53,** 2525–2545.

Kurihara, Y., and J. L. Holloway, 1967: Numerical integration of the nine-level global primitive equations model formulated by the box method. *Mon. Wea. Rev.,* **95,** 509–530.

Lamb, H., 1945: *Hydrodynamics.* Dover, 738 pp.

Leonard, B. P., 1991: The ULTIMATE conservative difference scheme applied to unsteady one-dimensional advection. *Comp. Meth. Appl. Mech. Eng.,* **88,** 17–74.

Levine, J., 1959: Spherical vortex theory of bubble-like motion in cumulus clouds. *J. Meteor.,* **16,** 653–662.

Lilly, D. K., 1962: On the numerical simulation of buoyant convection. *Tellus,* **14,** 168–172.

——, 1964: Numerical solutions for the shape-preserving two-dimensional thermal convection element. *J. Atmos. Sci.,* **21,** 83–98.

Ludlam, F. H., 1958: The hail problem. *Nubila,* **1,** 12–96.

Lugt, H. J., 1979: The dilemma of defining a vortex. *Recent Developments in Theoretical and Experimental Fluid Mechanics,* U. Müller, K. G. Roesner, and B. Schmidt, Eds., Springer-Verlag, 309–321.

Morton, B. R., 1997a: Discrete dry convective entities I: Review. *The Physics and Parameterization of Moist Atmospheric Convection,* R. K. Smith, Ed., Kluwer Academic, 143–173.

——, 1997b: Discrete dry convective entities II: Thermals and deflected jets. *The Physics and Parameterization of Moist Atmospheric Convection,* R. K. Smith, Ed., Kluwer Academic, 175–210.

——, G. I. Taylor, and J. S. Turner, 1956: Turbulent gravitational convection from maintained and instantaneous sources. *Proc. Roy. Soc. London,* **234A,** 1–23.

Ogura, Y., 1962: Convection of isolated masses of a buoyant fluid: A numerical calculation. *J. Atmos. Sci.,* **19,** 492–502.

——, 1963: The evolution of a moist convective element in a shallow, conditionally unstable atmosphere: A numerical calculation. *J. Atmos. Sci.,* **20,** 407–424.

Richards, J. M., 1961: Experiments on the penetration of an interface by buoyant thermals. *J. Fluid. Mech.,* **11,** 369–394.

Rotunno, R., 1981: On the evolution of thunderstorm rotation. *Mon. Wea. Rev.,* **109,** 577–586.

Rouse, H., C.-S. Yih, and H. W. Humphreys, 1952: Gravitational convection from a boundary source. *Tellus,* **4,** 201–210.

——, W. D. Baines, and H. W. Humphreys, 1953: Free convection over parallel sources of heat. *Proc. Phys. Soc.,* **66B,** 393–399.

Sánchez, O., D. J. Raymond, L. Libersky, and A. G. Petschek, 1989: The development of thermals from rest. *J. Atmos. Sci.,* **46,** 2280–2292.

Scorer, R. S., 1957: Experiments on convection of isolated masses of buoyant fluid. *J. Fluid. Mech.,* **2,** 583–594.

——, and F. H. Ludlum, 1953: Bubble theory of penetrative convection. *Quart. J. Roy. Meteor. Soc.,* **79,** 94–103.

Shapiro, A., and Y. Kogan, 1994: On vortex formation in multicell convective clouds in a shear-free environment. *Atmos. Res.,* **33,** 125–136.

Stommel, H., 1947: Entrainment of air into a cumulus cloud. *J. Meteor.,* **4,** 91–94.

——, 1951: Entrainment of air into a cumulus cloud II. *J. Meteor.,* **8,** 127–129.

Tao, W.-K., and J. Simpson, 1989: A further study of cumulus interactions and mergers: Three-dimensional simulations with trajectory analyses. *J. Atmos. Sci.,* **46,** 2974–3004.

Taylor, G. I., and A. E. Green, 1937: Mechanism of the production of small eddies from large ones. *Proc. Roy. Soc. London,* **158A,** 499–521.

Tremback, C. J., J. Powell, W. R. Cotton, and R. A. Pielke, 1987: The forward-in-time upstream advection scheme: Extension to higher orders. *Mon. Wea. Rev.,* **115,** 540–555.

Turner, J. S., 1957: Buoyant vortex rings. *Proc. Roy. Soc. London,* **239A,** 61–75.

——, 1962: The starting plume in neutral surroundings. *J. Fluid. Mech.,* **13,** 356–368.

——, 1963a: Model experiments relating to thermals with increasing buoyancy. *Quart. J. Roy. Meteor. Soc.,* **89,** 62–74.

——, 1963b: The motion of buoyant elements in turbulent surroundings. *J. Fluid. Mech.,* **16,** 1–16.

——, 1969: Buoyant plumes and thermals. *Ann. Rev. Fluid. Mech.,* **1,** 29–44.

——, 1986: Turbulent entrainment: The development of the entrainment assumption and its application to geophysical flows. *J. Fluid. Mech.,* **173,** 431–471.

Wilhelmson, R. B., and J. B. Klemp, 1978: A numerical study of storm splitting that leads to long-lived storms. *J. Atmos. Sci.,* **35,** 1974–1986.

Wilkens, E. M., Y. K. Sasaki, and R. H. Schauss, 1971a: Interactions between the velocity fields of successive thermals. *Mon. Wea. Rev.,* **99,** 215–226.

——, ——, and ——, 1971b: Vortex formation by successive thermals: A numerical calculation. *Mon. Wea. Rev.,* **99,** 577–592.

——, ——, and E. W. Marion, 1972: Laboratory simulation of wake effects on second and third thermals in a series. *Mon. Wea. Rev.,* **100,** 399–407.

——, ——, G. E. Gerber, and W. H. Chaplin Jr., 1976: Numerical simulation of the lateral interactions between buoyant clouds. *J. Atmos. Sci.,* **33,** 1321–1329.

Woodward, B., 1959: The motion in and around isolated thermals. *Quart. J. Roy. Meteor. Soc.,* **85,** 144–151.

Yih, C.-S., 1951: Free convection due to a point source of heat. *Proc. First U.S. Congr. Appl. Mech.,* E. Sternberg, Ed., American Society of Mechanical Engineers, 941–947.

——, 1977: Turbulent buoyant plumes. *Phys. Fluids* **20,** 1234–1237.

——, and F. Wu, 1981: Round buoyant laminar and turbulent plumes. *Phys. Fluids,* **24,** 794–801.